

9pm Cutoff 256x256 GaAs/Al_xGa_{1-x}As Quantum Well Infrared Photodetector Focal Plane Array Camera

S. D. Gunapala, J. K. Liu, M. Sundaram, J. S. Park*, C. A. Shott⁺, T. Hoelter⁺,
T. L. Lin^{**}, S. T. Massie⁺⁺, P. D. Maker, R. E. Muller, and G. Sarusi[#]

Center for Space Microelectronics Technology, Jet Propulsion Laboratory
California Institute of Technology, Pasadena, CA 91109

ABSTRACT

In this paper, we discuss the development of very sensitive long wavelength infrared (LWIR) GaAs/Al_xGa_{1-x}As quantum well infrared photodetectors (QWIPs), fabrication of random reflectors for efficient light coupling, and the demonstration of a LWIR 256x 256 focal plane array imaging camera. Excellent imagery, with a noise equivalent differential temperature (NEAT) of 25 mK has been achieved.

INTRODUCTION

There are several applications that require long wavelength, large, uniform, reproducible, low cost, low 1/f noise, low power dissipation, and radiation hard infrared (IR) focal plane arrays (FPAs). For example, the absorption lines of many gas molecules, such as ozone, water, carbon monoxide, carbon dioxide, and nitrous oxide occur in the wavelength region from 3 to 18 μ m. Thus, IR imaging systems that operate in the long wavelength IR (LWIR) region (6 -18 μ m) are required in many space applications such as monitoring the global atmospheric temperature profiles, relative humidity profiles, cloud characteristics, and the distribution of minor constituents in the atmosphere which are being planned for NASA's Earth Observing System [1]. In addition, 8 - 15 μ m FPAs would be very useful in detecting cold objects such as ballistic missiles in midcourse (when a hot rocket engine is not burning most of the emission peaks are in the 8-15 μ m IR region) [2]. The GaAs based Quantum Well Infrared Photodetector (QWIP) [3,4,5] is a potential candidate for such spaceborne and ground based applications and it can meet all of the requirements mentioned above for this spectral region.

Fig. 1 shows the schematic conduction band diagram of a typical *bound-to-continuum* QWIP [6] which utilizes bound-to-continuum intersubband absorption. By carefully designing the quantum well structure, as well as the light coupling to the detector, it is possible to optimize the material to have an optical response in the desired spectral range and determine the spectral response shape [7]. In QWIPs, the dark current originates from three different mechanisms [8]. As shown in Fig. 1, the dark current arising from the first process is due to quantum mechanical tunneling from well to well through the Al_xGa_{1-x}As barriers (sequential tunneling). This process is independent of temperature. Sequential tunneling dominates the dark current at very low

* Present address: Intel Corporation, Santa Clara, CA 95052

+ Amber, A Raytheon Company, Goleta, CA 93117

** Present address: Siliconix, Santa Clara, CA 95056

++ Quantum Epitaxial Designs, Inc., Bethlehem, PA 18015

Present address: elop-Electroptics Industries Ltd., Rehovot 76111 Israel

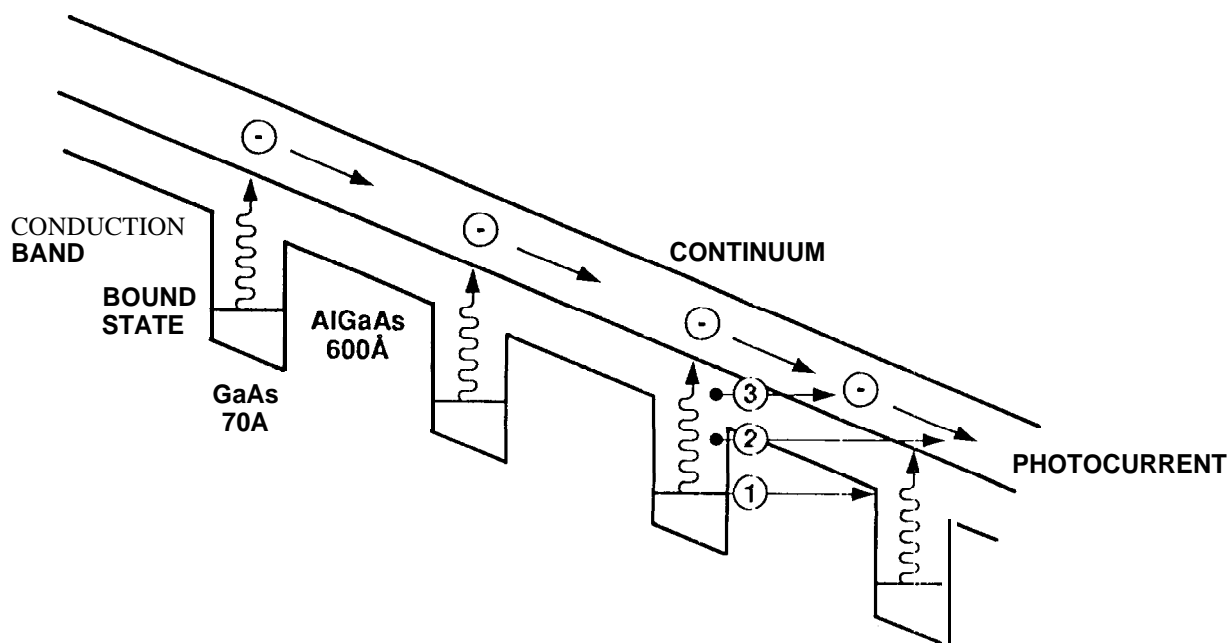


Fig. 1 Schematic diagram of the conduction band in a bound-to-continuum QWIP with an electric field. Absorption of IR photons can photoexcite electrons from the ground state of the quantum well into the continuum, causing a photocurrent. Three dark current mechanisms are also shown: ground state tunneling (1); thermally assisted tunneling (2); and thermionic emission (3).

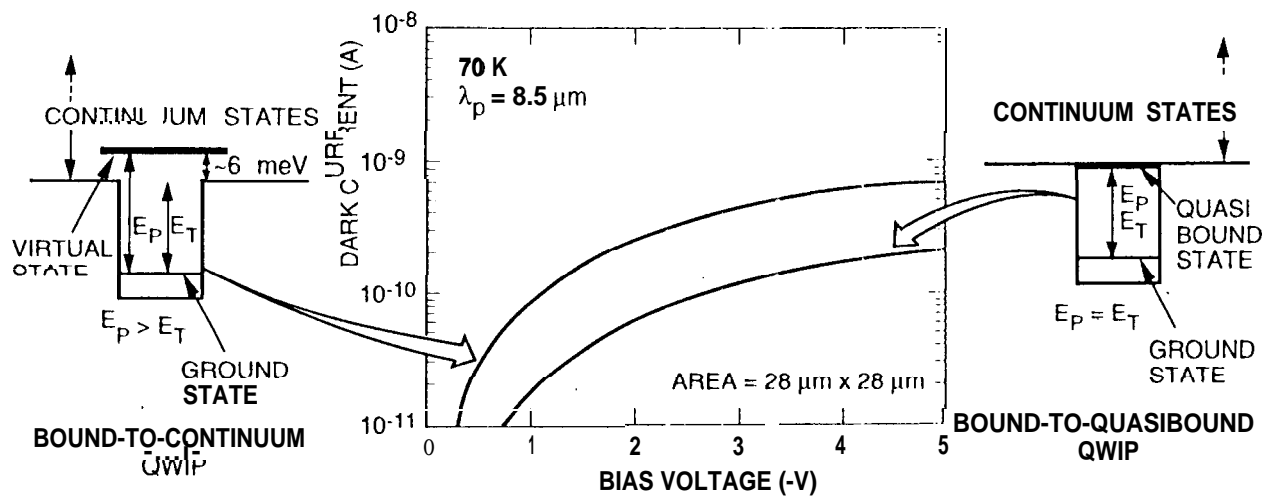


Fig. 2 Comparison of dark currents of bound-to-continuum and bound-to-quasibound LWIR QWIPs as a function of bias voltage at temperature $T = 70$ K. Data were taken with a $200 \mu\text{m}$ diam test structure and normalized to $28 \times 28 \mu\text{m}^2$ pixel.

temperatures (<30 K). The second mechanism is thermally assisted tunneling which involves a thermal excitation and tunneling through the tip of the barrier into the continuum energy levels. This process governs the dark current at medium temperatures. The third mechanism is classical thermionic emission and it dominates the dark current at higher temperatures (>55 K for $9\text{ }\mu\text{m}$ cutoff QWIPs). Consequently, for QWIPs operating at higher temperatures the last mechanism is the major source of dark current [8]. Therefore, the LWIR FPA we have discussed here in detail consisted of *bound-to-quasibound* QWIPs [9]. The advantage of the bound-to-quasibound QWIP over the bound-to-continuum QWIP [9] is that in the case of a bound-to-quasibound QWIP the energy barrier for thermionic emission is the same as it is for photoionization as shown in Fig. 2. In the case of the bound-to-continuum QWIP shown in Fig. 2 the energy barrier for the thermionic emission is about 6 meV less than the photoionization energy. Thus, the dark current of bound-to-quasibound QWIPs is reduced by a factor of 3 (i.e., $I_d \propto e^{-\frac{E_b}{kT}}$ for $T=70\text{ K}$) compared with bound-to-continuum QWIPs operating at the same peak wavelength.

TEST STRUCTURE RESULTS

The device structure consists of 50 periods, each period containing a $45\text{ }\text{\AA}$ well of GaAs (doped $n = 4 \times 10^{17}\text{ cm}^{-3}$) and a $500\text{ }\text{\AA}$ barrier of $\text{Al}_{0.3}\text{Ga}_{0.7}\text{As}$, sandwiched between $0.5\text{ }\mu\text{m}$ GaAs top and bottom contact layers doped $n = 5 \times 10^{17}\text{ cm}^{-3}$, grown on a semi-insulating GaAs substrate by molecular beam epitaxy (MBE). Then a $0.7\text{ }\mu\text{m}$ thick GaAs cap layer on top of a $300\text{ }\text{\AA}$ $\text{Al}_{0.3}\text{Ga}_{0.7}\text{As}$ stop-etch layer was grown *in situ* on top of the device structure to fabricate the light coupling optical cavity. The MBE grown QWIP structure was processed into $200\text{ }\mu\text{m}$ diameter mesa test structures (area = $3.14 \times 10^{-4}\text{ cm}^2$) using wet chemical etching, and Au/Ge ohmic contacts were evaporated onto the top and bottom contact layers. The dark current-voltage curves of the QWIP were measured as a function of temperature from $T = 30\text{--}90\text{ K}$ and the $T = 70\text{ K}$ curve

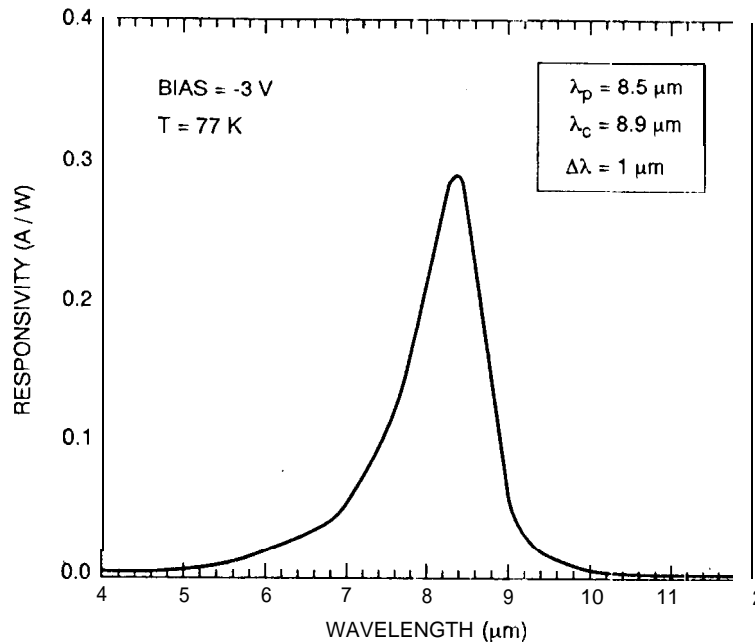


Fig. 3 Responsivity spectrum of a bound-to-quasibound LWIR QWIP test structure at temperature $T = 77\text{ K}$. The spectral response peak is at $8.5\text{ }\mu\text{m}$ and the long wavelength cutoff is at $8.9\text{ }\mu\text{m}$.

is shown in Fig. 2 with the dark current-voltage curve of a 8.5 μm peak bound-to-continuum QWIP. The virtual excited level of this bound-to-continuum QWIP is 6 meV above the $\text{Al}_x\text{Ga}_{1-x}\text{As}$ barrier. Theoretically this should give a factor of 3 higher dark current and it closely agrees with the experimental value of a factor of 4 higher dark current at bias $V_B = -2\text{V}$.

The responsivity spectra of these detectors were measured using a 1000 K blackbody source and a grating monochromator. The absolute peak responsivities R_p of the detectors were measured using a calibrated blackbody source. The detectors were back illuminated through a 45° polished facet [7] and a responsivity spectrum is shown in Fig. 3. The responsivity of the detector peaks at 8.5 μm and the peak responsivity (R_p) of the detector is 300 mA/W at bias $V_B = -3\text{ V}$. The spectral width and the cutoff wavelength are $\Delta\lambda/\lambda = 10\%$ and $\lambda_c = 8.9\mu\text{m}$ respectively. The bias dependent peak responsivity of the detector is shown in Fig. 4. The measured absolute peak responsivity of the detector is small up to about $V_B = -0.5\text{ V}$. Beyond that it increases nearly linearly with bias reaching $R_p = 380\text{ mA/W}$ at $V_B = -5\text{ V}$. This type of behavior of responsivity versus bias is typical for a bound-to-quasibound QWIP. The peak quantum efficiency was 7% at bias $V_B = -1\text{ V}$ (lower quantum efficiency is due to the lower well doping density) for a 45° double pass.

The current noise i_n was measured using a spectrum analyzer and the photoconductive gain g was experimentally determined using [10] $g = i_n^2 / 4eI_D B + 1/2N$, where B is the measurement band width and N is the number of quantum wells. The photoconductive gain of the detector reached 0.98 at $V_B = -5\text{ V}$. Since the gain of QWIP is inversely proportional to the number of quantum wells N , the better comparison would be the well capture probability p_c , which is directly related to the gain [11] by $g = 1/Np_c$. The calculated well capture probabilities are 25 % at

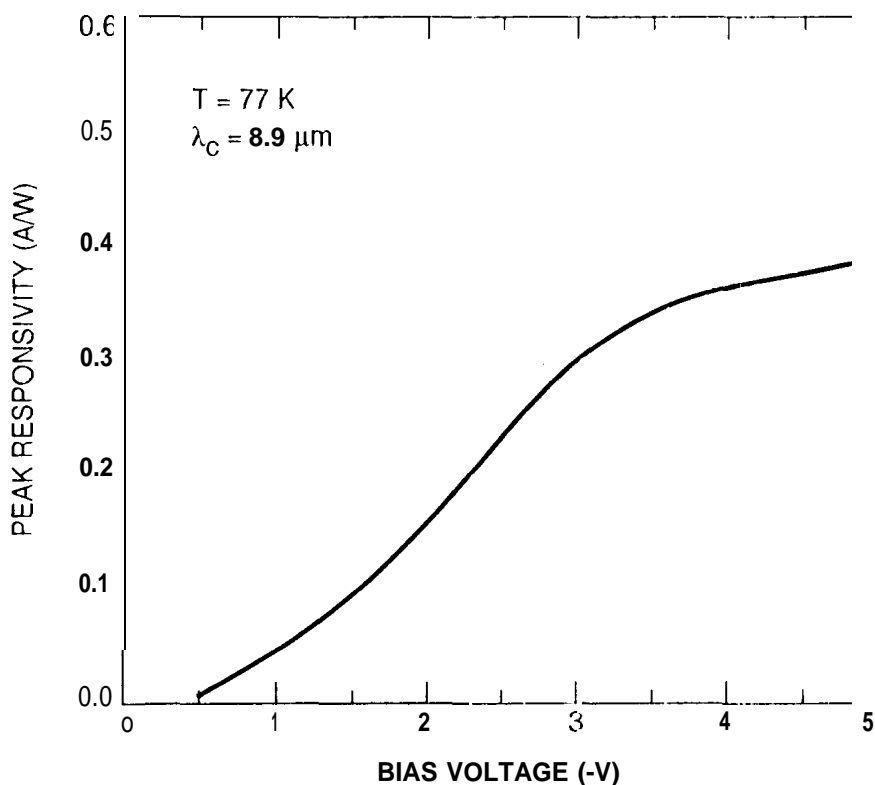


Fig. 4 Peak responsivity as a function of bias voltage at temperature $T = 77\text{ K}$.

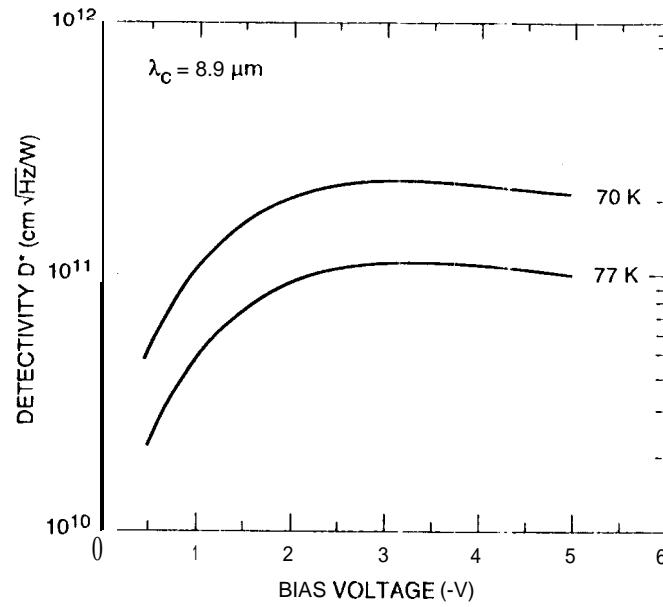


Fig. 5 Detectivity as a function of bias voltage at temperatures $T = 70$ and 77 K .

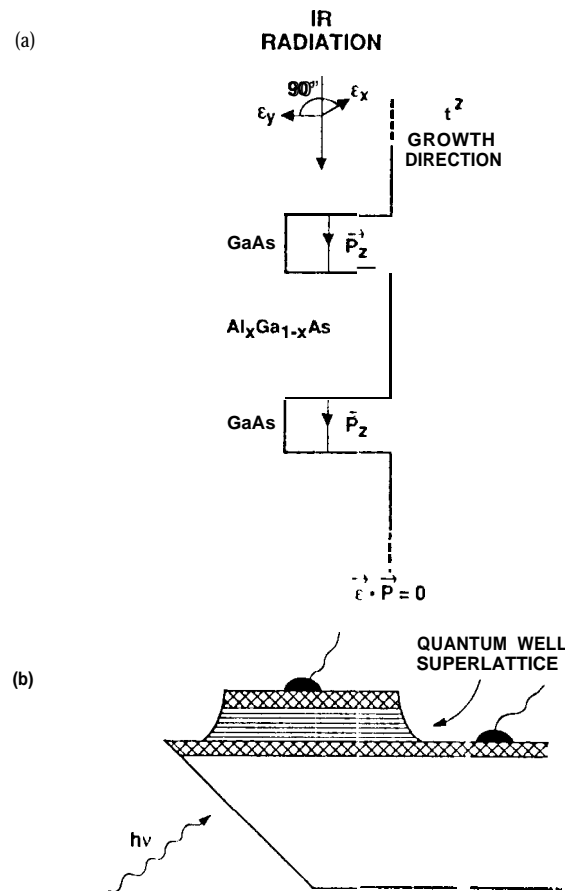


Fig. 6 (a) Intersubband absorption process of QWIPs at normal incidence. (b) 45° polished facet light coupling.

low bias (i.e., $V_B = -1$ V) and 2% at high bias (i.e., $V_B = -5$ V) which together indicate the excellent hot-electron transport in this device structure. The peak defectivity is defined as $D_p^* = R_p \sqrt{AB} / i_n$, where R_p is the peak responsivity, A is the area of the detector and $A = 3.14 \times 10^{-4} \text{ cm}^2$. The measured peak defectivity at bias $V_B = -3.2$ V and temperature $T = 70$ K is $2.3 \times 10^{11} \text{ cm}^2/\text{Hz/W}$.

LIGHT COUPLING

QWIPs do not absorb radiation incident normal to the surface since the light polarization must have an electric field component normal to the superlattice (growth direction) to be absorbed by the confined carriers. As shown in Fig. 6(a) when the incoming light contains no polarization component along the growth direction, the matrix element of the interaction vanishes (i.e., $\vec{E} \cdot \vec{p}_z = 0$ where \vec{E} is the polarization and \vec{p}_z is the momentum along the z direction). As a consequence, these detectors have to be illuminated through a 45° polished facet [7] as shown in Fig. 6(b). Clearly, this illumination scheme limits the configuration of detectors to linear arrays and single elements. For imaging, it is necessary to be able to couple light uniformly to two dimensional arrays of these detectors.

Many more passes of IR light inside the detector structure can be obtained by incorporating a randomly roughened reflecting surface on top of the detectors which also removes the light coupling limitations and makes two dimensional QWIP imaging arrays feasible. A factor of eight enhancement in QWIP responsivity compared to 45° illumination geometry has been achieved with a randomly roughened reflecting surface [11]. The random structure on top of the detector prevents the light from being diffracted normally backward after the second bounce as happens in the case of cross-grating. After each bounce, light is scattered at a different random angle and the only chance for light to escape out of the detector is when it is reflected towards the surface within the critical angle of the normal. For the GaAs/air interface this angle is about 17°, defining a very narrow escape cone for the trapped light. The reflector was designed with two levels of scattering surfaces located at quarter wavelength separations, as shown in Fig. 7. The area of the top unetched

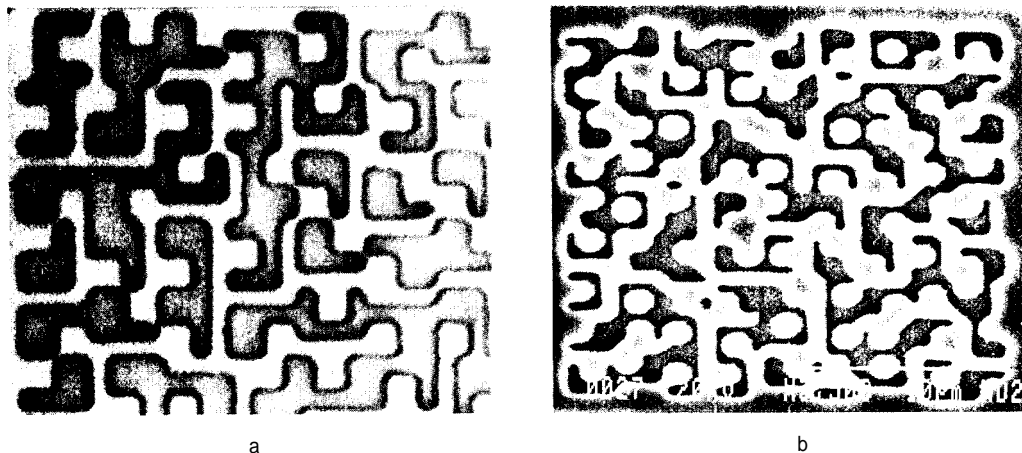


Fig. 7 (a) Two level random reflector on a pixel ($38 \times 38 \mu\text{m}^2$) of $15 \mu\text{m}$ cutoff QWIP FPA. The minimum feature size is $1.25 \mu\text{m}$. (b) Two level random reflector on a pixel ($28 \times 28 \mu\text{m}^2$) of $9 \mu\text{m}$ cutoff QWIP FPA. The minimum feature size is $0.6 \mu\text{m}$. This random reflector was less sharp and had fewer scattering centers when compared to Fig. 7(a) due to the difficulties associated with sub-micron photolithography.

level is equal to the area of the etched level ($\lambda_{\text{GaAs}}/4$ deep). Therefore, the normally reflected light intensities from the top and bottom surfaces of random reflector are equal and 180° out of phase, thus maximizing the destructive interference at normal reflection and hence lowering the light leakage through the escape cone. This random structure was fabricated on the detectors by using standard photolithography and CCl_2F_2 selective dry etching. The advantage of the photolithographic process over a completely random process is the ability to accurately control the feature size and preserve the pixel to pixel uniformity which is a prerequisite for high sensitivity imaging FPAs.

IMAGING ARRAYS

Figures 7(a) and 7(b) show random reflectors on a pixel of $15\mu\text{m}$ cutoff 128×128 and $9\mu\text{m}$ cutoff 256×256 QWIP FPAs respectively. The minimum feature size of the random reflectors of $15\mu\text{m}$ cutoff and $9\mu\text{m}$ cutoff FPAs were $1.25\mu\text{m}$ and $0.6\mu\text{m}$ respectively. As shown in Fig. 7(b) the random reflectors of the $9\mu\text{m}$ cutoff FPA were less sharp and had fewer scattering centers compared to Fig. 7(a) and this is due to the difficulties associated with sub-micron photolithography. After the random reflector array was defined by the lithography and dry etching, the photoconductive QWIPs of the 256×256 FPAs were fabricated by wet chemical etching through the photosensitive $\text{GaAs}/\text{Al}_x\text{Ga}_{1-x}\text{As}$ multi-quantum well layers into the $0.5\mu\text{m}$ thick doped GaAs bottom contact layer. The pitch of the FPA is $38\mu\text{m}$ and the actual pixel size is $28 \times 28\mu\text{m}^2$. Then the random reflectors on top of the detectors were covered with Au/Ge and Au for Ohmic contact and reflection. Figure 8 shows twenty five processed QWIP FPAs on a 3 inch GaAs wafer. Then iridium bumps were evaporated on top of the detectors for Si readout circuit (ROC) hybridization. A single QWIP FPA was chosen and hybridized (via iridium bump-bonding process) to a 256×256 Si multiplexer (Amber AE-166) and biased at $V_B = -1.0\text{ V}$. The FPA was back-illuminated through the flat thinned substrate membrane (thickness $\approx 1300\text{ \AA}$). This initial array gave excellent images with 99.98% of the pixels working (number of dead pixels ≈ 10), demonstrating the high yield of GaAs technology.

We have used the following equation to calculate the noise equivalent temperature difference NEAT of the FPA.

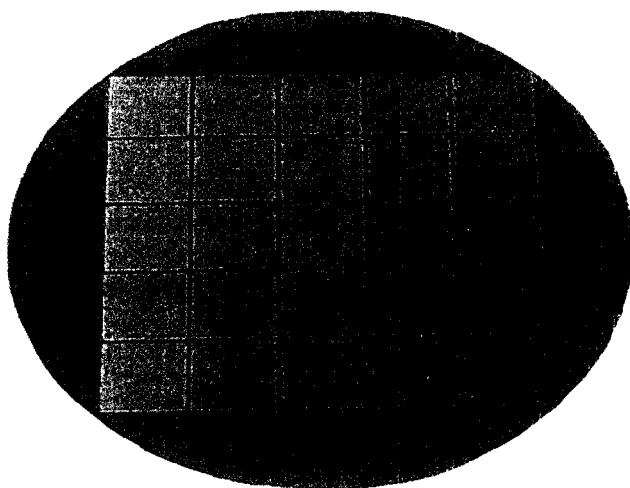


Fig. 8 Twenty five 256×256 QWIP focal plane arrays on a 3 in. GaAs wafer.

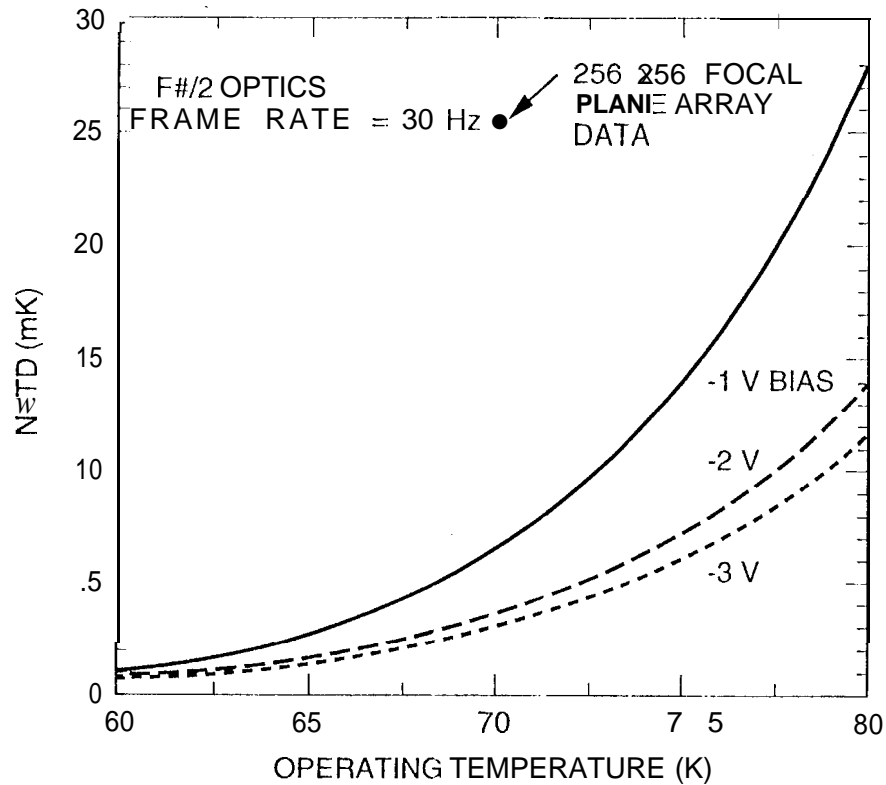


Fig. 9 Noise equivalent temperature difference NEAT estimated from test structure data as a function of temperature for bias voltages $V_B = -1$, -2 , and -3 V. The background temperature $T_B = 300$ K and the area of the pixel $A = (28 \mu\text{m})^2$. The measured NEAT of the focal plane array is 25 mK at an operating temperature of 70 K and bias $V_B = -1$ V.

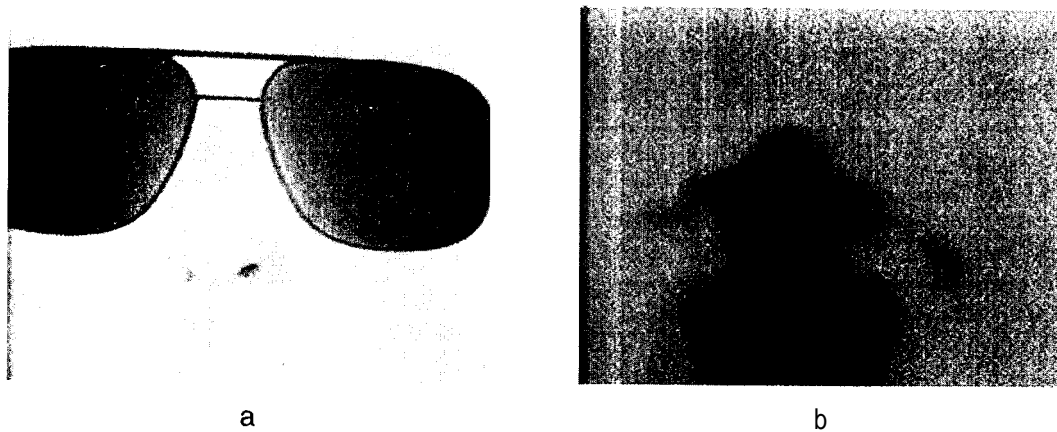


Fig. 10 (a) One frame of video image taken with the $9 \mu\text{m}$ cutoff 256x256 QWIP camera, The tiny dark squares on each frame of the glasses are the reflections of coldFPA in the camera, (b) An absorption image of acetone fumes (acetone has a strong IR absorption at $8.8 \mu\text{m}$) taken with a $9 \mu\text{m}$ cutoff 256x256 QWIP FPA camera.

$$\text{NEAT} = \frac{\sqrt{AB}}{D_B^* (dP_B / dT)} \quad (1)$$

where D_B^* is the blackbody defectivity and dP_B / dT is the derivative of the integrated blackbody power with respect to temperature. Figure 9 shows the NEAT of the FPA estimated from the test structure data as a function of temperature for bias voltages $V_B = -1, -2$, and -3 V and the frame rate of 30 Hz. The background temperature $T_B = 300$ K and the area of the pixel $A = (28 \mu\text{m})^2$. The measured mean NFAT of the FPA was 25 mK at an operating temperature of $T = 70$ K and bias $V_B = -1$ V for 300 K background. This reasonably agrees with our estimated value of 7 mK based on test structure data. The peak quantum efficiency of the FPA was 9.5% (much lower quantum efficiency than expected can be attributed to the poor grating fill factor) and this corresponds to an average of 3 passes of IR radiation through the photosensitive multi-quantum well region. The uncorrected photocurrent uniformity (pixel-to-pixel) of the 65,536 pixels of the 256x256 FPA is about 7% ($= \text{sigma}/\text{mean}$). The uniformity after two point (17° and 27° Celsius) correction was 0.05 %. As mentioned earlier this high yield is due to the excellent GaAs growth uniformity and the mature GaAs processing technology.

Video images were taken at a frame rate of 30 Hz with f/2 anti-reflection coated germanium optics at temperatures as high as $T = 70$ K, using a ROC capacitor having a charge capacity of 9×10^6 electrons. Figure 10 (a) shows one frame of a video image taken with a $9 \mu\text{m}$ cutoff 256x256 QWIP camera. The 2 tiny dark squares on the glasses are the reflections of cold FPA of the camera. Figure 10(b) shows an absorption image of acetone fumes (acetone has a strong IR absorption at $8.8 \mu\text{m}$) taken with the same camera. These images demonstrate the high sensitivity of the 256x256 QWIP staring array camera,

No band pass filters were used and are unnecessary in QWIP camera systems because of the narrow spectral response of QWIPs. It should be noted that these initial unoptimized FPA results are far from optimum. The gratings were not optimized (as described earlier) for maximum light coupling efficiency; no microlenses were used; no antireflection coatings were used on the backside of the FPA; and finally the multiplexer used was a photovoltaic InSb multiplexer which is certainly not optimized to supply the proper bias and impedance levels required by photoconductive QWIPs. Implementation of these improvements should significantly enhance the QWIP FPA operating temperature (i.e., 77 K for $9 \mu\text{m}$).

ACKNOWLEDGMENTS

We are grateful to C. A. Kukkonen, V. Sarohia, S. K. Khanna, K. M. Koliwad, T. N. Krabach, and P. J. Grunthaler of the Jet Propulsion Laboratory, D. Duston and L. Caveny of the Ballistic Missile Defense Organization, and G. Johnston of the National Aeronautics and Space Administration (NASA) Headquarters for encouragement and support of this work. The research described in this paper was performed by the Center for Space Microelectronics Technology, Jet Propulsion Laboratory, California Institute of Technology, and was jointly sponsored by the BMDO/IS&T Office, and the NASA Office of Space Access and Technology.

References

- [1] M. T. Chahine, "Sensor requirements for Earth and Planetary Observations," *Proceedings of Innovative Long Wavelength Infrared Detector Workshop*, Pasadena, California, pp. 3-31, April 24-26, 1990.

- [2] D. Duston, "BMDO's IS&T faces new hi-tech priorities," *BMD Monitor*, pp. 180-183, May 19, 1995.
- [3] C. G. Bethea, B. F. Levine, M. T. Asom, R. E. Leibenguth, J. W. Stayt, K. G. Glogovsky, R. A. Morgan, J. D. Blackwell, and W. J. Parrish, "Long Wavelength Infrared 128 x 128 $\text{Al}_x\text{Ga}_{1-x}\text{As}/\text{GaAs}$ Quantum Well Infrared Camera and Imaging System," *IEEE Trans. Electron. Devices*, vol. 40, pp. 1957-1963, 1993.
- [4] L. J. Kozlowski, G. M. Williams, G. J. Sullivan, C. W. Farley, R. J. Andersson, J. Chen, D. T. Cheung, W. E. Tennant, and R. E. DeWames, "1.2 μm Wavelength Infrared 128x128 $\text{GaAs}/\text{AlGaAs}$ Multiple Quantum Well Hybrid Focal Plane Array," *IEEE Trans. Electron. Devices*, vol. ED-38, pp. 1124-1130, 1991.
- [5] W. A. Beck, T. S. Faska, J. W. Little, J. Albritton, and M. Sensiper, *Proceedings of the Second International Symposium on 2-20 μm Wavelength Infrared Detectors and Arrays: Physics and Applications*, October 10-12, 1994, Miami Beach, Florida.
- [6] B. F. Levine, C. G. Bethea, G. Hasnain, V. O. Shen, E. Pelve, R. R. Abbott, and S. J. Hsieh, "High sensitivity y low dark current 10 μm GaAs quantum well infrared photodetectors," *Appl. Phys. Lett.*, vol. 56, pp. 851-853, 1990.
- [7] B. F. Levine, "Quantum Well Infrared Photodetectors," *J. Appl. Phys.*, vol. 74, pp. R1-R81, 1993.
- [8] Sarath Gunapala, Gabby Sarusi, Jin Park, True-I on Lin, and Barry Levine, "Infrared Detectors Reach New Lengths," *Physics World*, pp. 35-40, December, 1994.
- [9] S. D. Gunapala, J. S. Park, G. Sarusi, T. L. Lin, J. K. Liu, P. D. Maker, R. E. Muller, C. A. Shott, T. Hoelter, and B. F. Levine "128 x 128 $\text{GaAs}/\text{Al}_x\text{Ga}_{1-x}\text{As}$ Quantum Well Infrared Photodetector Focal Plane Array for Imaging at 15 μm ," submitted to *IEEE Electron Device Letters*.
- [10] W. A. Beck, "Photoconductive gain and generation-recombination noise in multiple-quantum-well infrared detectors," *Appl. Phys. Lett.*, vol. 63, pp. 3589-3591, 1993.
- [11] G. Sarusi, B. F. Levine, S. J. Pearton, K. M. S. V. Bandara, and R. E. Leibenguth, "Improved performance of quantum well infrared photodetectors using random scattering optical coupling," *Appl. Phys. Lett.*, vol. 64, pp. 960-962, 1994.

9 μ m Cutoff 256x256 GaAs/Al_xGa_{1-x}As Quantum Well Infrared Photodetector Focal Plane Array Camera

S. D. Gunapala, J. K. Liu, M. Sundaram, J. S. Park, C. A. Shott, T. Hoelter, T. L. Lin, S. T. Massie, P. D. Maker, R. E. Muller, and G. Sarusi

ABSTRACT

In this paper, we discuss the development of very sensitive long, wavelength infrared (LWIR) GaAs/Al_xGa_{1-x}As quantum well infrared photodetectors (QWIPs), fabrication of random reflectors for efficient light coupling, and the demonstration of a LWIR 256 x 256 focal plane array imaging camera. Excellent imagery, with a noise equivalent differential temperature (NE Δ T) of 25 mK has been achieved,

S. D. Gunapala, J. K. Liu, M. Sundaram, P. D. Maker, and R. E. Muller are with Center for Space Microelectronics Technology, Jet Propulsion Laboratory, California Institute of Technology, Pasadena, CA 91109.

J. S. Park was with Jet Propulsion Laboratory, Pasadena, CA 91109. He is now with Intel Corporation, Santa Clara, CA 95052.

C. A. Shott and T. Hoelter are with Amber, A Raytheon Company, Goleta, CA 93117.

T. L. Lin was with Jet Propulsion Laboratory, Pasadena, CA 91109. He is now with Siliconix, Santa Clara, CA 95056.

S. T. Massie is with Quantum Epitaxial Designs, inc., Bethlehem, PA 18015.

G. Sarusi was with Jet Propulsion Laboratory, Pasadena, CA 91109. He is now with Elop-Electroptics industries Ltd., Rehovot 76111 Israel.

Introduction

There are several applications that require long wavelength, large, uniform, reproducible, low cost, low $1/f$ noise, low power dissipation, and radiation hard infrared (IR) focal plane arrays (FPAs). For example, the absorption lines of many gas molecules, such as ozone, water, carbon monoxide, carbon dioxide, and nitrous oxide occur in the wavelength region from 3 to 18 μm . Thus, IR imaging systems that operate in the long wavelength IR (LWIR) region (6 - 18 μm) are required in many space applications such as monitoring the global atmospheric temperature profiles, relative humidity profiles, cloud characteristics, and the distribution of minor constituents in the atmosphere which are being planned for NASA's Earth Observing System [1]. In addition, 8- 15 μm FPAs would be very useful in detecting cold objects such as ballistic missiles in midcourse (when a hot rocket engine is not burning most of the emission peaks are in the 8-15 μm IR region) [2]. The GaAs based Quantum Well Infrared Photodetector (QWIP) [3,4,5] is a potential candidate for such spaceborne and ground based applications and it can meet all of the requirements mentioned above for this spectral region.

Fig. 1 shows the schematic conduction band diagram of a typical *bound-to-continuum* QWIP [6] which utilizes bound-to-continuum intersubband absorption. By carefully designing the quantum well structure, as well as the light coupling to the detector, it is possible to optimize the material to have an optical response in the desired spectral range and determine the spectral response shape [7]. In QWIPs, the dark current originates from three different mechanisms [8]. As shown in Fig. 1, the dark current arising from the first process is due to quantum mechanical tunneling from well to well through the $\text{Al}_x\text{Ga}_{1-x}\text{As}$ barriers (sequential tunneling). This process is independent of temperature. Sequential tunneling dominates the dark current at very low temperatures ($<30\text{ K}$). The second mechanism is thermally assisted tunneling which involves a thermal excitation and tunneling through the tip of the barrier into the continuum energy levels. This process governs the dark current at medium temperatures. The third mechanism is classical thermionic emission and it dominates the dark current at higher temperatures ($>55\text{ K}$ for 9 μm cutoff QWIPs). Consequently, for QWIPs operating at higher temperatures the last mechanism is the major source of dark current [8]. Therefore, the LWIR FPA we have discussed here in detail consisted of *bound-to-quasibound* QWIPs [9]. The advantage of the bound-to-quasibound QWIP over the bound-to-continuum QWIP [9] is that in the case of a bound-to-quasibound QWIP the energy barrier for

thermionic emission is the same as it is for photoionization as shown in Fig. 2. In the case of the bound-to-continuum QWIP shown in Fig. 2 the energy barrier for the thermionic emission is about 6 meV less than the photoionization energy. Thus, the dark current of bound-to-quasibound QWIPs is reduced by a factor of 3 (i.e., $I_d \propto e^{-\frac{E_b}{kT}} \approx e^{-1}$ for $T = 70$ K) compared with bound-to-continuum QWIPs operating at the same peak wavelength.

Test Structure Results

The device structure consists of 50 periods, each period containing a 45 Å well of GaAs (doped $n = 4 \times 10^{17} \text{ cm}^{-3}$) and a 500 Å barrier of $\text{Al}_{0.3}\text{Ga}_{0.7}\text{As}$, sandwiched between 0.5 μm GaAs top and bottom contact layers doped $n = 5 \times 10^{17} \text{ cm}^{-3}$, grown on a semi-insulating GaAs substrate by molecular beam epitaxy (MBE). Then a 0.7 μm thick GaAs cap layer on top of a 300 Å $\text{Al}_{0.3}\text{Ga}_{0.7}\text{As}$ stop-etch layer was grown *in situ* on top of the device structure to fabricate the light coupling optical cavity. The MBE grown QWIP structure was processed into 200 μm diameter mesa test structures (area = $3.14 \times 10^{-4} \text{ cm}^2$) using wet chemical etching, and Au/Ge ohmic contacts were evaporated onto the top and bottom contact layers. The dark current-voltage curves of the QWIP were measured as a function of temperature from $T = 30$ -90 K and the $T = 70$ K curve is shown in Fig. 2 with the dark current-voltage curve of a 8.5 μm peak bound-to-continuum QWIP. The virtual excited level of this bound-to-continuum QWIP is 6 meV above the $\text{Al}_x\text{Ga}_{1-x}\text{As}$ barrier. Theoretically this should give a factor of 3 higher dark current and it closely agrees with the experimental value of a factor of 4 higher dark current at bias $V_B = -2\text{V}$.

The responsivity spectra of these detectors were measured using a 1000 K blackbody source and a grating monochromator. The absolute peak responsivities (R_p) of the detectors were measured using a calibrated blackbody source. The detectors were back illuminated through a 45° polished facet [7] and a responsivity spectrum is shown in Fig. 3. The responsivity of the detector peaks at 8.5 μm and the peak responsivity (R_p) of the detector is 300 mA/W at bias $V_B = -3\text{V}$. The spectral width and the cutoff wavelength are $\Delta\lambda / \lambda = 10\%$ and $\lambda_c = 8.9 \mu\text{m}$ respectively. The bias dependent peak responsivity of the detector is shown in Fig. 4. The measured absolute peak responsivity of the detector is small up to about $V_B = -0.5\text{V}$. Beyond that it increases nearly linearly with bias reaching $R_p = 380 \text{ mA/W}$ at $V_B = -5\text{V}$. This type of behavior of responsivity versus bias is typical for a bound-to-quasibound QWIP. The peak quantum efficiency was

6.9% at bias $V_B = -1$ V (lower quantum efficiency is due to the lower well doping density) for a 45° double pass.

The current noise i_n was measured using a spectrum analyzer and the photoconductive gain g was experimentally determined using $i_n^2 / 4eI_D B + 1/2N$, where B is the measurement band width and N is the number of quantum wells. The photoconductive gain of the detector reached 0.98 at $V_B = -5$ V. Since the gain of QWIP is inversely proportional to the number of quantum wells N , the better comparison would be the well capture probability p_c , which is directly related to the gain [11] by $g = 1/Np_c$. The calculated well capture probabilities are 25% at low bias (i.e., $V_B = -1$ V) and 2% at high bias (i.e., $V_B = -5$ V) which together indicate the excellent hot-electron transport in this device structure. The peak defectivity is defined as $D_p^* = R_p \sqrt{AB} / i_n$, where R_p is the peak responsivity, A is the area of the detector and $A = 3.14 \times 10^{-4} \text{ cm}^2$. The measured peak defectivity at bias $V_B = -3.2$ V and temperature $T = 70$ K is $2.3 \times 10^{11} \text{ cm}^2/\text{Hz/W}$. These detectors show background limited performance (BLIP) at bias $V_B = -2$ V and temperature $T = 72$ K for 300 K background with $f/2$ optics.

light Coupling

QWIPs do not absorb radiation incident normal to the surface since the light polarization must have an electric field component normal to the superlattice (growth direction) to be absorbed by the confined carriers. As shown in Fig. 6(a) when the incoming light contains no polarization component along the growth direction, the matrix element of the interaction vanishes (i.e., $\vec{E} \cdot \vec{p}_z = 0$ where \vec{E} is the polarization and \vec{p}_z is the momentum along the z direction). As a consequence, these detectors have to be illuminated through a 45° polished facet [7] as shown in Fig. 6(b). Clearly, this illumination scheme limits the configuration of detectors to linear arrays and single elements. For imaging, it is necessary to be able to couple light uniformly to two dimensional arrays of these detectors.

Many more passes of IR light inside the detector structure can be obtained by incorporating a randomly roughened reflecting surface on top of the detectors which also removes the light coupling limitations and makes two dimensional QWIP imaging arrays feasible. A factor of eight enhancement in QWIP responsivity compared to 45° illumination geometry has been achieved with a randomly roughened reflecting surface [11]. The random structure on top of the detector prevents the light from being diffracted

normally backward after the second bounce as happens in the case of cross-grating. After each bounce, light is scattered at a different random angle and the only chance for light to escape out of the detector is when it is reflected towards the surface within the critical angle of the normal. For the GaAs/air interface this angle is about 17° , defining a very narrow escape cone for the trapped light. The reflector was designed with two levels of scattering surfaces located at quarter wavelength separations, as shown in Fig. 7. The area of the top unetched level is equal to the area of the etched level ($\lambda_{\text{GaAs}}/4$ deep). Therefore, the normally reflected light intensities from the top and bottom surfaces of random reflector are equal and 180° out of phase, thus maximizing the destructive interference at normal reflection and hence lowering the light leakage through the escape cone. This random structure was fabricated on the detectors by using standard photolithography and CCl_2F_2 selective dry etching. The advantage of the photolithographic process over a completely random process is the ability to accurately control the feature size and preserve the pixel to pixel uniformity which is a prerequisite for high sensitivity imaging FPAs.

imaging Arrays

Figures 7(a) and 7(b) show random reflectors on a pixel of $15\ \mu\text{m}$ cutoff 128×128 and $9\ \mu\text{m}$ cutoff 256×256 QWIP FPAs respectively. The minimum feature size of the random reflectors of $15\ \mu\text{m}$ cutoff and $9\ \mu\text{m}$ cutoff FPAs were $1.25\ \mu\text{m}$ and $0.6\ \mu\text{m}$ respectively. As shown in Fig. 7(b) the random reflectors of the $9\ \mu\text{m}$ cutoff FPA were less sharp and had fewer scattering centers compared to Fig. 7(a) and this is due to the difficulties associated with sub-micron photolithography. After the random reflector array was defined by the lithography and dry etching, the photoconductive QWIPs of the 256×256 FPAs were fabricated by wet chemical etching through the photosensitive GaAs/ $\text{Al}_x\text{Ga}_{1-x}\text{As}$ multi-quantum well layers into the $0.5\ \mu\text{m}$ thick doped GaAs bottom contact layer. The pitch of the FPA is $38\ \mu\text{m}$ and the actual pixel size is $28 \times 28\ \mu\text{m}^2$. Then the random reflectors on top of the detectors were covered with Au/Ge and Au for Ohmic contact and reflection. Figure 8 shows twenty five processed QWIP FPAs on a 3 inch GaAs wafer. Then iridium bumps were evaporated on top of the detectors for Si readout circuit (ROC) hybridization. A single QWIP FPA was chosen and hybridized (via iridium bump-bonding process) to a 256×256 CMOS multiplexer (Amber AR-166) and biased at $V_B = -1.0\ \text{V}$. At temperatures below $72\ \text{K}$, the signal to noise ratio of the system is limited by array non-uniformity, multiplexer readout noise, and photo current (photon flux) noise. At temperatures above $72\ \text{K}$, temporal noise due to the QWIP's higher dark

current becomes the limitation. As mentioned earlier this higher dark current is due to thermionic emission and which causes the charge storage capacitors of the readout **circuitry to saturate**. Since the QWIP is a high impedance device, it should yields a very high charge injection coupling efficiency into the integration capacitor of the multiplexer. In fact Bethea *et al.* [3] have demonstrated charge injection efficiencies approaching 90%. Charge injection efficiency can be obtained from [4]

$$\eta_{inj} = \frac{g_m R_{Det}}{1 + g_m R_{Det}} \left(1 - \frac{1}{1 + g_m R_{Det}} \right) \quad (1)$$

where g_m is the transconductance of the MOSFET and it is given by $g_m = eI_{Det}/kT$. The differential resistance R_{Det} of the pixels at -1 V bias is 4.5×10^0 Ohms at $T=70$ K and detector capacitance C_{Det} is 3.0×10^{-14} F. The detector dark current $I_{Det} = 14$ pA at same operation condition. According to the equation (1) the charge injection efficiency $\eta_{inj}=99\%$ at a frame rate of 30 Hz. The FPA was back-illuminated through the flat thinned substrate membrane (thickness ≈ 1300 Å). This initial **array gave excellent** images with 99.98% of the pixels working (number of dead pixels ≈ 10), demonstrating the high yield of GaAs technology.

We have used the following equation to calculate the noise equivalent temperature difference NE Δ T of the FPA.

$$NE\Delta T = \frac{\sqrt{AB}}{D_b^* (dP_b / dT) \sin^2(\theta/2)} \quad (2)$$

where D_b^* is the blackbody detectivity, dP_b / dT is the derivative of the integrated blackbody power with respect to temperature, and θ is the field of view angle [i.e., $\sin^2(\theta/2) = (4f^2 + 1)^{-1}$, where f is the f number of the optical system]. Figure 9 shows the NE Δ T of the FPA estimated from the test structure data as a function of temperature for bias voltages $V_B = -1, -2$, and -3 V. The background temperature $T_B = 300$ K, the area of the pixel $A = (28 \mu m)^2$, the f number of the optical system is 2, and the frame rate is 30 Hz. The measured mean NE Δ T of the FPA was 25 mK at an operating temperature of $T = 70$ K and bias $V_B = -1$ V for 300 K background. This reasonably agrees with our estimated value of 7 mK based on test structure data. The peak quantum efficiency of the FPA was 3 % (much lower quantum efficiency than expected can be attributed to the poor

grating fill factor) and this corresponds to an average of 3 passes of IR radiation (equivalent to single 45° pass) through the photosensitive multi-quantum well region, As shown in Fig. 10 the uncorrected photocurrent non-uniformity (which include 1 % non-uniformity of ROC and 1.4% non-uniformity due to the cold-stop not being able give the same field of view to all the pixels in the FPA) of the 65,536 pixels of the 256x256 FPA is about 6.8% ($= \text{sigma}/\text{mean}$). The non-uniformity after two point (1 $^\circ$ and 27 $^\circ$ Celsius) correction was 0.05%, As mentioned earlier this high yield is due to the excellent GaAs growth uniformity and the mature GaAs processing technology.

Video images were taken at a frame rate of 30Hz with f/2 anti-reflection coated germanium optics at temperatures as high as $T = 70$ K, using a ROC capacitor having a charge capacity of 9×10^6 electrons. Figure 11(a) shows one frame of a video image taken with a 9 μm cutoff 256x256 QWIP camera. The 2 tiny dark squares on the glasses are the reflections of cold FPA of the camera. Figure 10(b) shows an absorption image of **acetone** fumes (acetone has a strong IR absorption at 8.8 μm) taken with the same camera. These images demonstrate the high sensitivity of the 256x256 QWIP staring array camera.

No band pass filters were used and are unnecessary in QWIP camera systems because of the narrow spectral response of QWIPs. It should be noted that these initial unoptimized FPA results are far from optimum. The gratings were not optimized (as described earlier) for maximum light coupling efficiency; no microlenses were used; no antireflection coatings were used on the backside of the FPA; and finally the multiplexer used was a photovoltaic InSb multiplexer which is certainly not optimized to supply the proper bias and impedance levels required by photoconductive QWIPs. implementation of these improvements should significantly enhance the QWIP FPA operating temperature (i.e., 77 K for 9 μm).

Acknowledgments

We are grateful to C. A. Kukkonen, V. Sarohia, S. K. Khanna, K. M. Koliwad, T. N. Krabach, and P. J. Grunthaner of the Jet Propulsion Laboratory, D. Duston and L. Caveny of the Ballistic Missile Defense Organization, and G. Johnston of the National Aeronautics and Space Administration (NASA) Headquarters for encouragement and support of this work. The research described in this paper was performed by the Center

for Space Microelectronics Technology, Jet Propulsion Laboratory, California Institute of Technology, and was jointly sponsored by the BMDO/IS&T Office, and the NASA Office of Space Access and Technology.

References

- [1] M. T. Chahine, "Sensor requirements for Earth and Planetary Observations," *Proceedings of Innovative Long Wavelength Infrared Detector Workshop*, Pasadena, California, pp. 3-31, April 24-26, 1990.
- [2] D. Duston, "BM DOS IS&T faces new hi-tech priorities," *BMD Monitor*, pp. 180-183, May 19, 1995.
- [3] C. G. Bethea, B. F. Levine, M. T. Asom, R. E. Leibenguth, J. W. Stayt, K. G. Glogovsky, R. A. Morgan, J. D. Blackwell, and W. J. Parrish, "Long Wavelength Infrared 128 x 128 Al_xGa_{1-x}As/GaAs Quantum Well Infrared Camera and Imaging System," *IEEE Trans. Electron. Devices*, vol. 40, pp. 1957-1963, 1993.
- [4] L. J. Kozlowski, G. M. Williams, G. J. Sullivan, C. W. Farley, R. J. Andersson, J. Chen, D. T. Cheung, W. E. Tennant, and R. E. DeWames, "128x 128 GaAs/AlGaAs Multiple Quantum Well Hybrid Focal Plane Array," *IEEE Trans. Electron. Devices*, vol. ED-38, pp. 1124-1130, 1991.
- [5] W. A. Beck, T. S. Faska, J. W. Little, J. Albritton, and M. Sensiper, *Proceedings of the Second International Symposium on 2-20 μm Wavelength Infrared Detectors and Arrays: Physics and Applications*, October 10-12, 1994, Miami Beach, Florida.
- [6] B. F. Levine, C. G. Bethea, G. Hasnain, V. O. Shen, E. Pelve, R. R. Abbott, and S. J. Hsieh, "High sensitivity low dark current 10 μm GaAs quantum well infrared photodetectors," *Appl. Phys. Lett.*, vol. 56, pp. 851-853, 1990.
- [7] B. F. Levine, "Quantum Well Infrared Photodetectors," *J. Appl. Phys.*, vol. 74, pp. R1-R81, 1993.
- [8] Sarath Gunapala, Gabby Sarusi, Jin Park, True-hm Lin, and Barry Levine, "Infrared Detectors Reach New Lengths," *Physics World*, pp. 35-40, December, 1994.

- [9] S. D. Gunapala, J. S. Park, G. Sarusi, T. L. Lin, J. K. Liu, P. D. Maker, R. E. Muller, C. A. Shell, 'I'. Hoelter, and B. F. Levine "128 x 128 GaAs/Al_xGa_{1-x}As Quantum Well infrared Photodetector Focal Plane Array for Imaging at 15 μ m," submit ted to *IEEE Electron Device Letters*.
- [10] W. A. Beck, "Photoconductive gain and generation-recombination noise in multiple-quantum- well in frared detectors, " *Appl. Phys. Lett.*, VOL. 63, pp. 3589-3591, 1993.
- [11] G. Sarusi, B. F. Levine, S. J. Pear[on, K. M. S. V. Bandara, and R. E. Leibenguth, "Improved performance of quantum well infrared photodetectors using random scattering optical coupling," *Appl. Phys. Lett.*, vol. 64, pp. 960-962., 1994.

FIGURE CAPTIONS

Fig. 1 Schematic diagram of the conduction band in a bound-to-continuum QWIP with an electric field. Absorption of 1 R photons can photoexcite electrons from the ground state of the quantum well into the continuum, causing a photocurrent. Three dark current mechanisms are also shown: ground state tunneling (1); thermally assisted tunneling (2); and thermionic emission (3).

Fig. 2 Comparison of dark currents of bound-to-continuum and bound-to-quasibound LWIR QWIPs as a function of bias voltage at temperature $T = 70$ K. Data were taken with a 200 μm diam test structure and normalized to $28 \times 28 \mu\text{m}^2$ pixel.

Fig. 3 Responsivity spectrum of a bound-to-quasibound LWIR QWIP test structure at temperature $T = 77$ K. The spectral response peak is at $8.5 \mu\text{m}$ and the long wavelength cutoff is at $8.9 \mu\text{m}$.

Fig. 4 Peak responsivity as a function of bias voltage at temperature $T = 77$ K.

Fig. 5 Detectivity as a function of bias voltage at temperatures $T = 70$ and 77 K.

Fig. 6 (a) Intersubband absorption process of QWIPs at normal incidence. (b) 45° polished facet light coupling.

Fig. 7 (a) Two level random reflector on a pixel ($38 \times 38 \mu\text{m}^2$) of $15 \mu\text{m}$ cutoff QWIP FPA. The **minimum feature size** is 1.25 μm . (b) Two level random reflector on a pixel ($28 \times 28 \mu\text{m}^2$) of 9 μm cutoff QWIP FPA. The minimum feature size is 0.6 μm . This random reflector was less sharp and had fewer scattering centers when compared to Fig. 7(a) due to the difficulties associated with sub-micron photolithography.

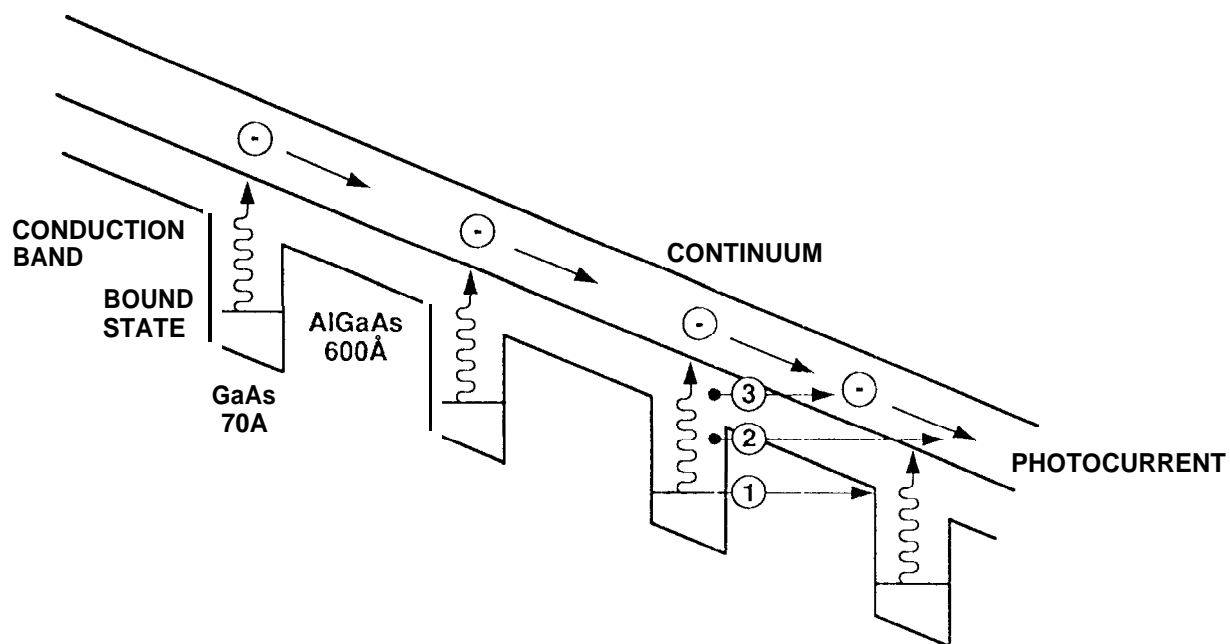
Fig. 8 Twenty five 256×256 QWIP focal plane arrays on a 3 in. GaAs wafer.

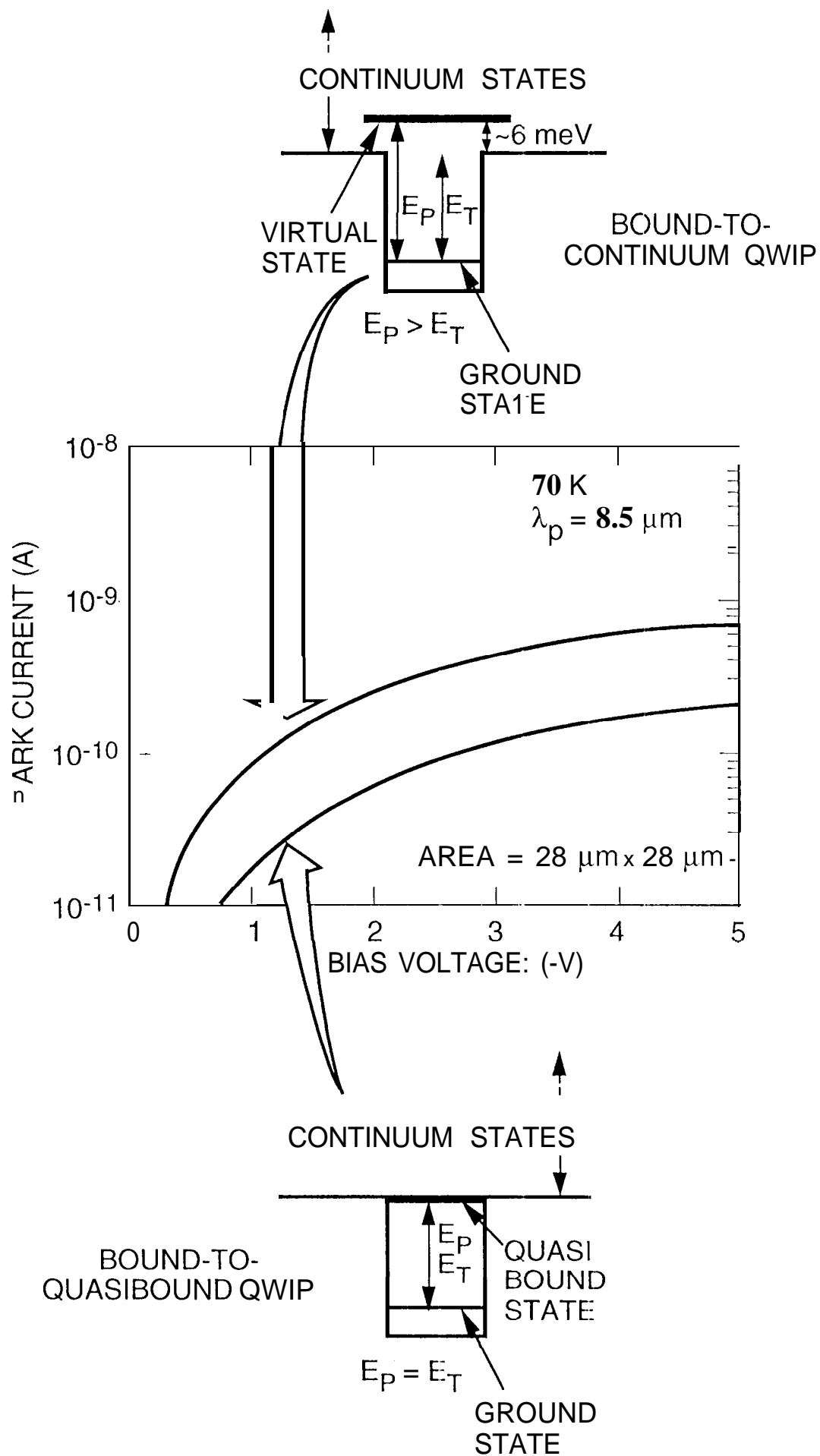
Fig. 9 Noise equivalent temperature difference NEAT estimated from test structure data as a function of temperature for bias voltages $V_B = -1, -2, \text{ and } -3$ V. The

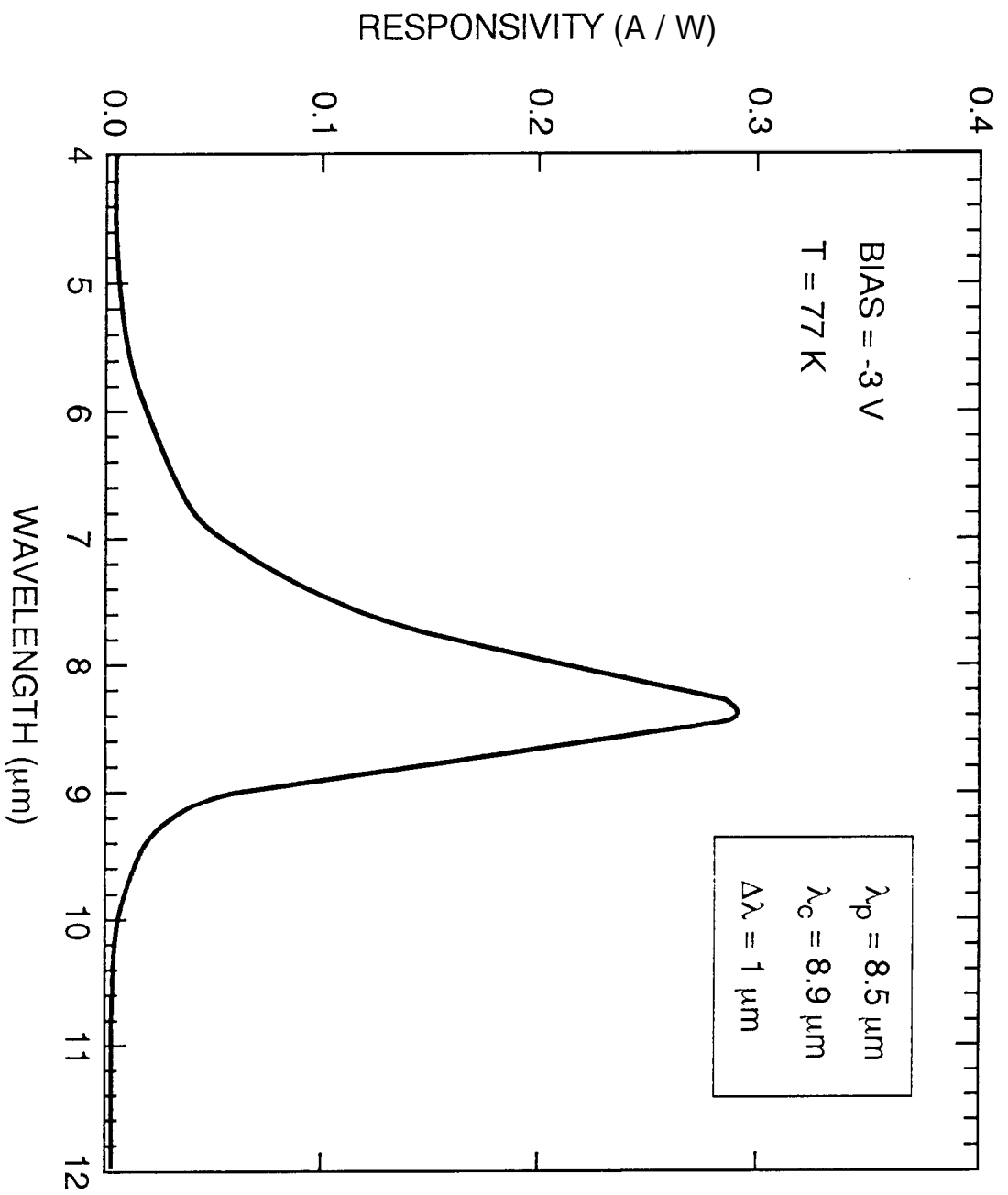
background temperature $T_B = 300$ K and the area of the pixel $A = (28 \mu\text{m})^2$. The measured $N\hbar\Delta T$ of the focal plane array is 25 mK at an operating temperature of 70 K and bias $V_B = -1$ V.

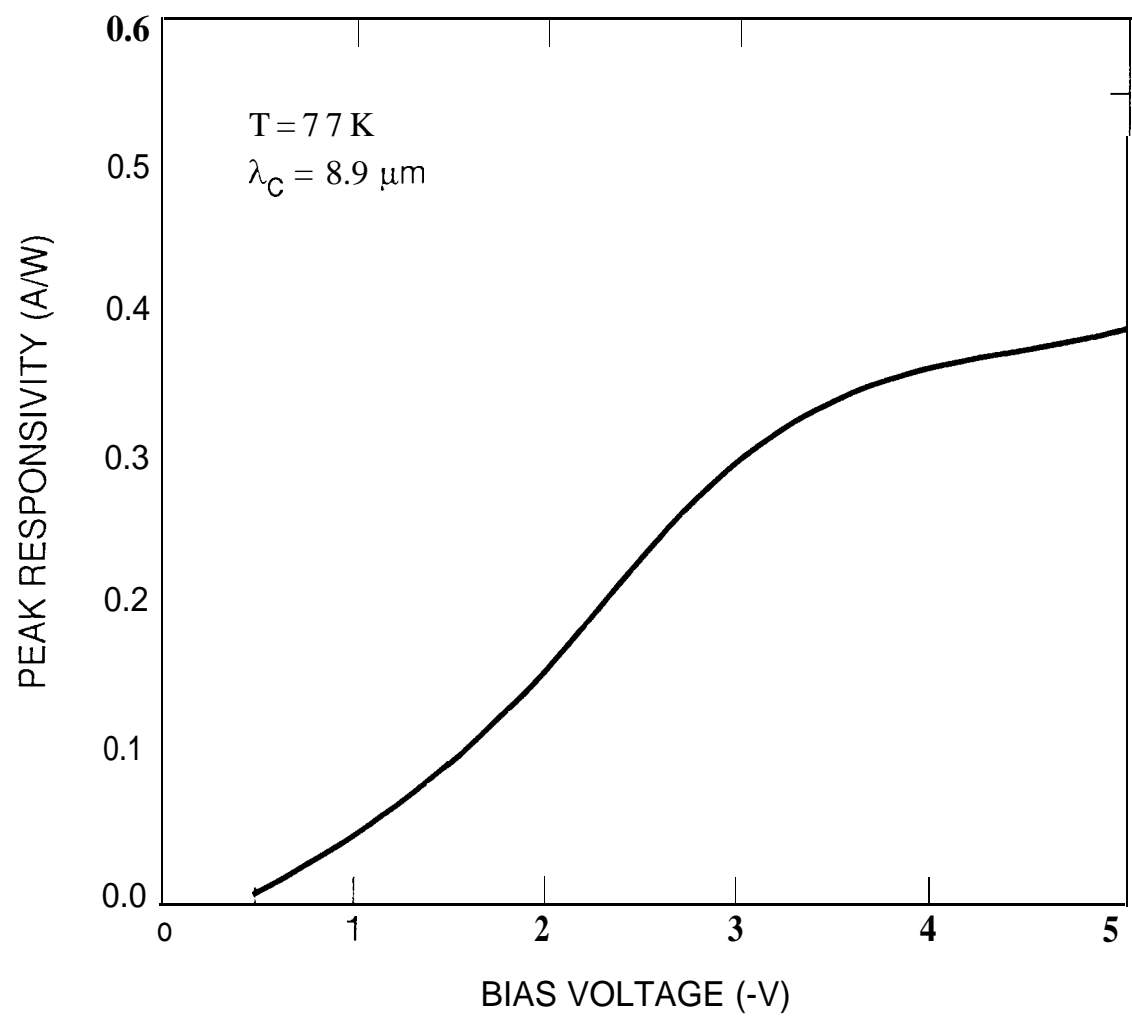
Fig. 10 Photosignal histogram of the 65,536 pixels of the 256x256 array showing a high uniformity of the FPA. The uncorrected non-uniformity (= standard deviation/mean) of the FPA is only 6.8% including 1 % non-uniformity of ROC and 1.4% non-uniformity due to the cold-stop not being able give the same field of view to all the pixels in the FPA.

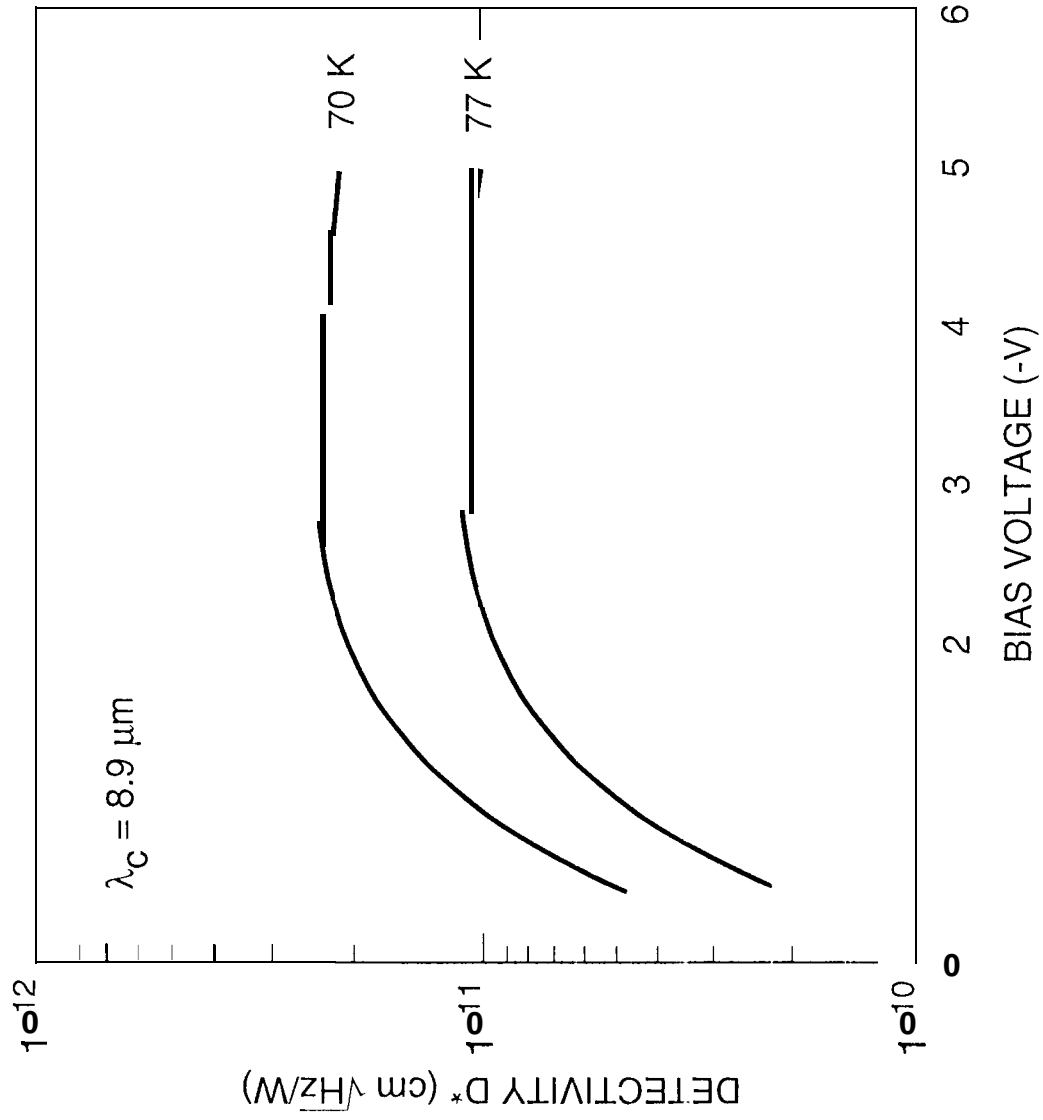
Fig. 1 (a) One frame of video image taken with the 9 μm cutoff 256x256 QWIP camera. The tiny dark squares on each frame of the glasses are the reflections of cold FPA in the camera. (b) An absorption image of acetone fumes (acetone has a strong IR absorption at 8.8 μm) taken with a 9 μm cutoff 256x256 QWIP FPA camera.





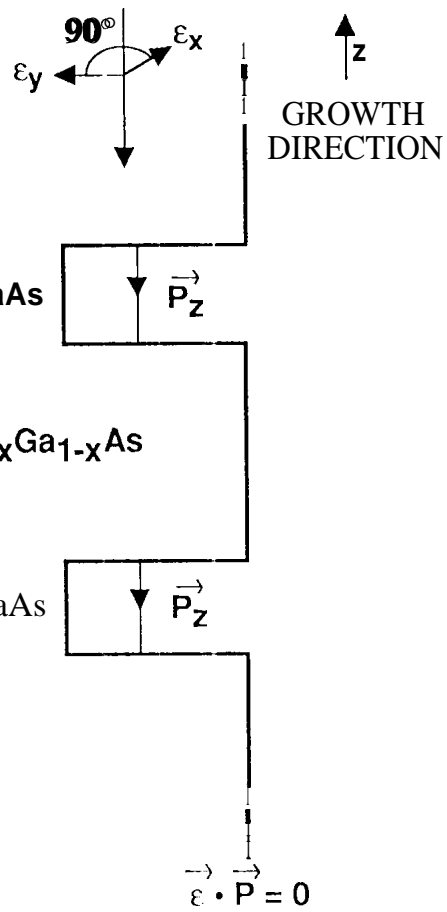




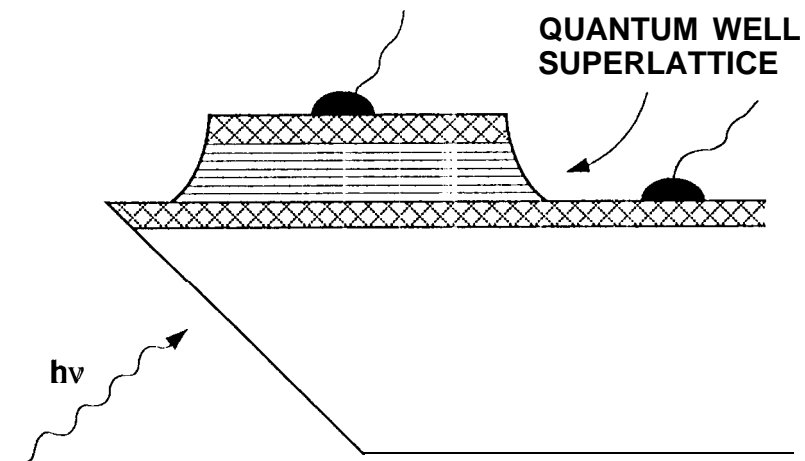


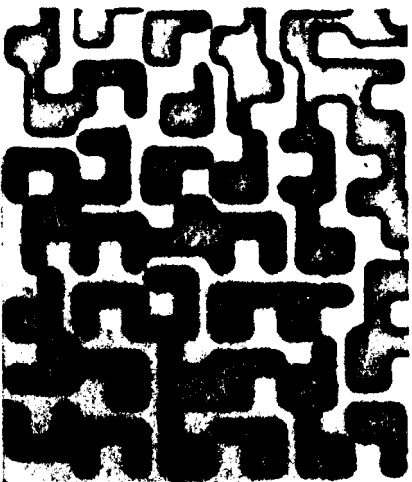
(a)

IR
RADIATION

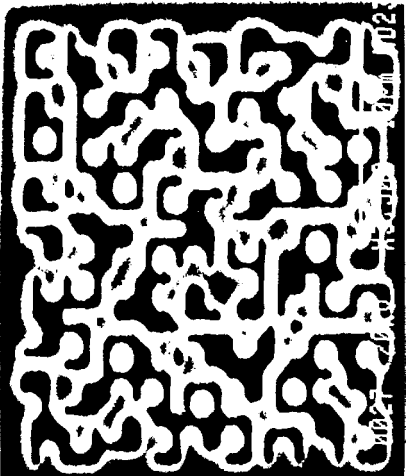


(b)

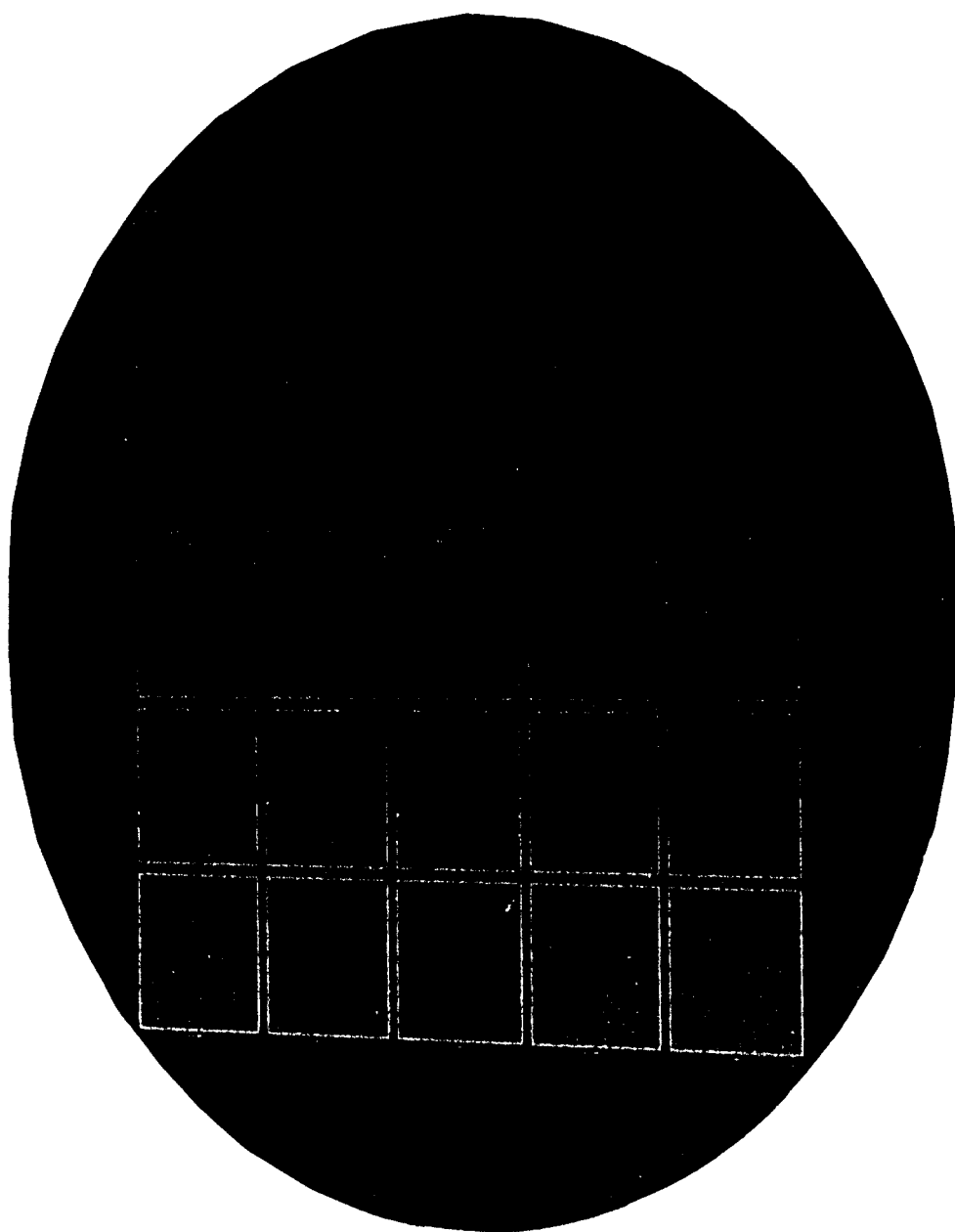


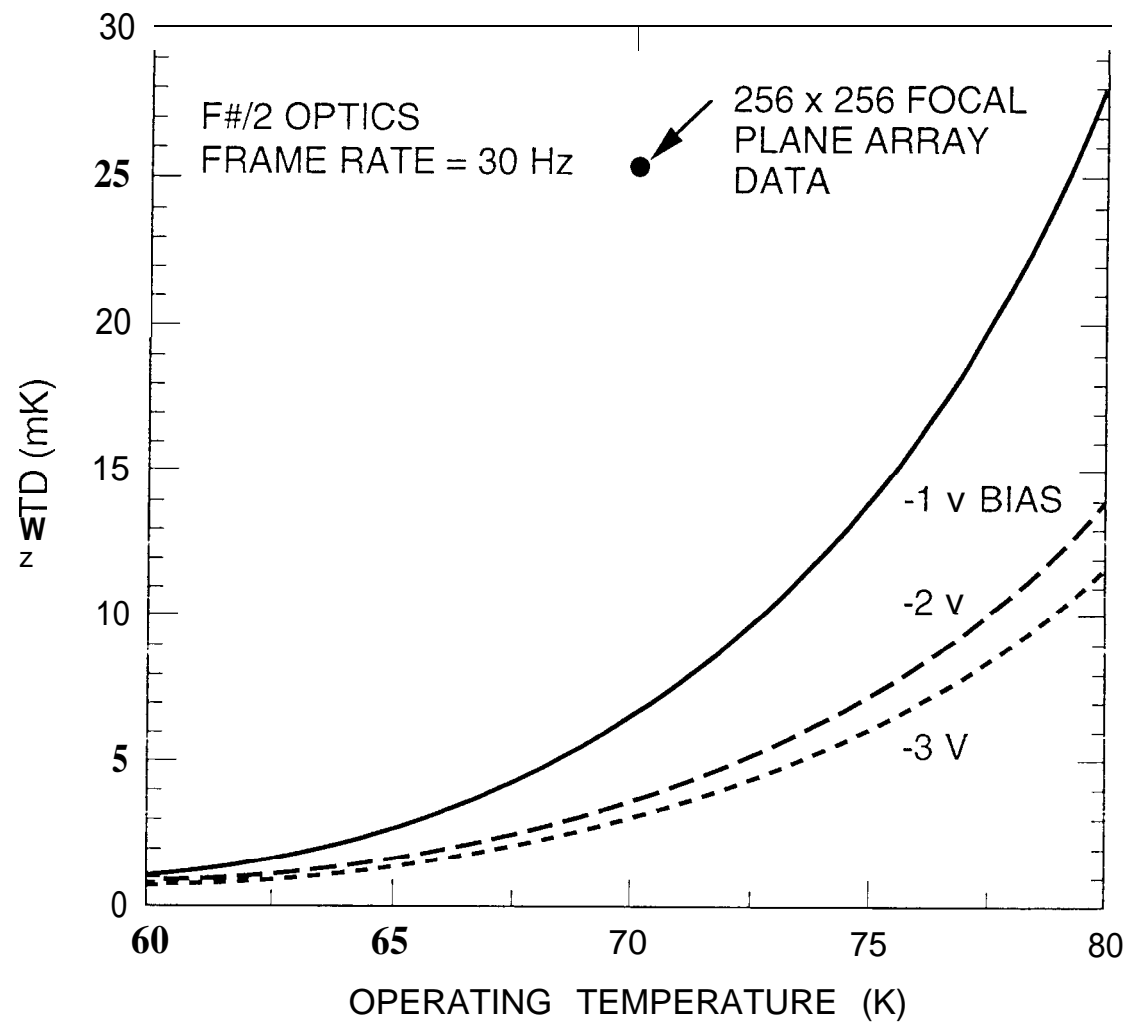


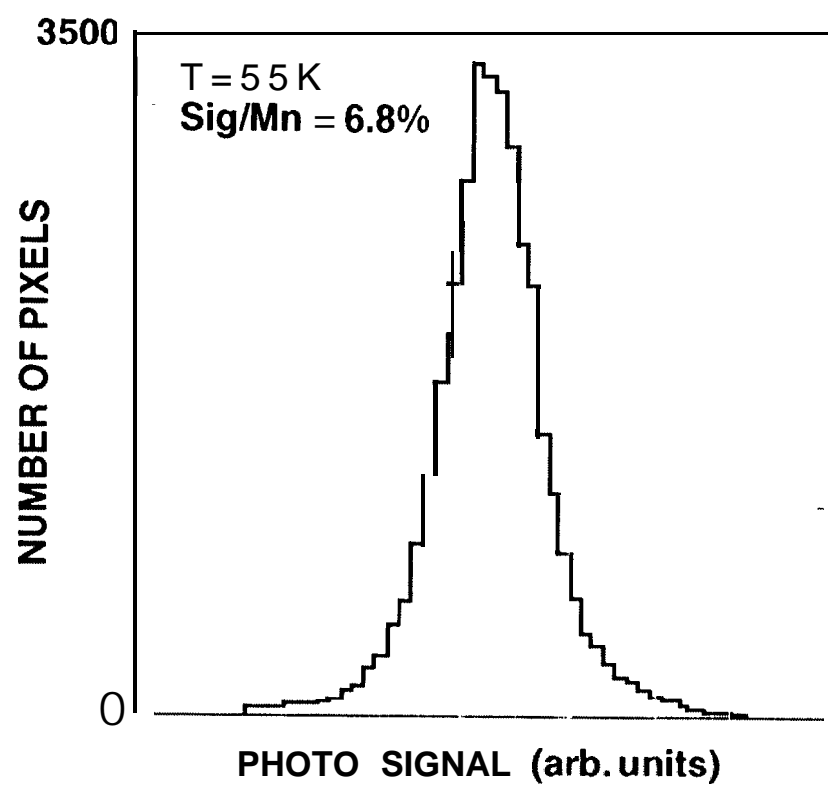
a



b

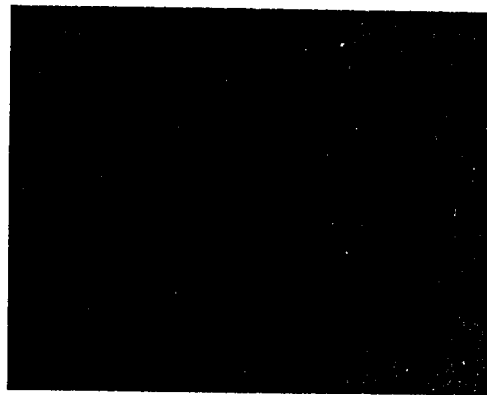








a



b